

# Magnetic Topological Transistor

Hai-Peng Sun,<sup>1,\*</sup> Chang-An Li,<sup>1,†</sup> Song-Bo Zhang,<sup>2</sup> Hai-Zhou Lu,<sup>3,4</sup> and Björn Trauzettel<sup>1,5</sup>

<sup>1</sup>*Institute for Theoretical Physics and Astrophysics,  
University of Würzburg, 97074 Würzburg, Germany*

<sup>2</sup>*Department of Physics, University of Zürich, Winterthurerstrasse 190, 8057, Zürich, Switzerland*

<sup>3</sup>*Shenzhen Institute for Quantum Science and Engineering and Department of Physics,  
Southern University of Science and Technology (SUSTech), Shenzhen, 518055, China*

<sup>4</sup>*Shenzhen Key Laboratory of Quantum Science and Engineering, Shenzhen, 518055, China*

<sup>5</sup>*Würzburg-Dresden Cluster of Excellence ct.qmat, Germany*

(Dated: June 23, 2022)

We propose a magnetic topological transistor based on  $\text{MnBi}_2\text{Te}_4$ , in which the “on” state (quantized conductance) and the “off” state (zero conductance) can be easily switched by changing the relative direction of two adjacent electric fields (parallel vs. antiparallel) applied within a two-terminal junction. We explain that the magnetic topological transistor relies on a novel mechanism due to the interplay of topology, magnetism, and structure inversion asymmetry induced by the external electric fields. Its performance depends substantially on film thickness and type of magnetic order. We show that “on” and “off” states of the transistor are robust against disorder due to the topological nature of the surface states. Moreover, we reveal that Berry curvature matters in thin-film devices.

**Introduction.**— Topological insulators (TIs) are bulk insulators with topological Dirac surface states protected by time-reversal symmetry [1–3]. Soon after the realization of TIs, serious efforts have been made to exploit the role of topology in fabricating field-effect transistors [4, 5]. Breaking time-reversal symmetry by magnetic doping in TIs, this opens a sizable gap in the spectrum of the Dirac surface states. This gap allows for the realization of topological transistors [6–8], which could be elementary building blocks in topological electronics. Topological transistors may also be realized by exploiting topological phase transitions [9–14].

Recently, the intrinsic antiferromagnetic TI  $\text{MnBi}_2\text{Te}_4$  has been discovered [15–34], which exhibits large magnetic surface gaps ( $\sim 70$  meV) [16] and high mobilities ( $>1000$   $\text{cm}^2/\text{Vs}$ ) [35, 36]. While extensive research efforts have been devoted to the topological electronic structure of the  $\text{MnBi}_2\text{Te}_4$  family [16–18, 37–46], their transport properties remain largely unexplored despite of some magnetotransport measurements [34–36, 47–53]. Recent studies have revealed that electric fields work as convenient knobs to control the transport properties of  $\text{MnBi}_2\text{Te}_4$  [33–35].

In this Letter, we propose a new on/off switching mechanism to realize a magnetic topological transistor based on antiferromagnetic  $\text{MnBi}_2\text{Te}_4$ . This mechanism relies on three crucial ingredients: (i) topological Dirac surface states, (ii) exchange fields, and (iii) external electric fields. To elucidate the physical picture, we first construct an effective model for  $\text{MnBi}_2\text{Te}_4$  thin films in presence of external electric fields. We then show that manipulating the direction of electric fields allows us to selectively address the transport of top and bottom Dirac surface states. Exploiting this feature, we propose a two-terminal magnetic topological transistor. The “on” state (quantized conductance) and the “off” state (zero con-

ductance) of this device are selected by the relative directions of two adjacent electric fields [Figs. 1(a)-(b)]. The physical reason is that we are able to guide the electron transport from the top surface state of the left region to either the top surface state of the right region (“on” state) or to the bottom surface state of the right region (“off” state). We show below that high on-off ratios ( $\sim 10^7$ ) of the magnetic topological transistor can be achieved when the antiferromagnetic  $\text{MnBi}_2\text{Te}_4$  films satisfy one of two criteria: (i) The films are thick enough

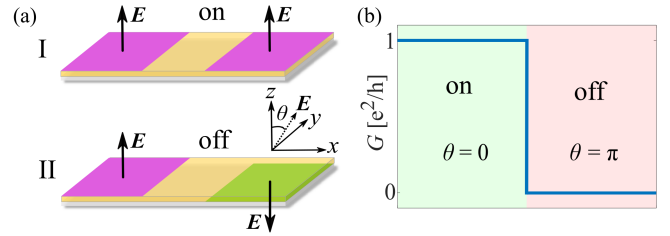


FIG. 1. (a) Schematic of a magnetic topological transistor based on magnetic TIs. The magnetic TI (yellow) is grown on a substrate (grey). Two independent electric fields are applied to two neighboring regions. The external electric field in the left region is fixed along  $z$ -direction. The angle  $\theta$  describes the relative angle of the two independent electric fields. For case I, the electric field in the right region is parallel to that in the left region and the transistor is in the “on” state. For case II, the electric field in the right region is antiparallel to that in the left region and the transistor is in the “off” state. The purple and green colors represent the dominant surface states crossing the Fermi level at top and bottom of the sample, respectively. (b) Two-terminal conductance of the magnetic topological transistor that switches from “on” (quantized conductance) to “off” (zero conductance) as the relative direction of the electric fields changes from parallel ( $\theta = 0$ ) to antiparallel ( $\theta = \pi$ ).

to avoid hybridization of top and bottom surface states. (ii) The films have compensated antiferromagnetic order. In the latter case, the transistor can tolerate a considerable hybridization of top and bottom surface states due to their opposite Berry curvature.

**Effective model for surface states.**— To demonstrate that the electric field can be exploited to select a particular surface state transport, we first construct an effective model of antiferromagnetic  $\text{MnBi}_2\text{Te}_4$  thin films in presence of an electric field.  $\text{MnBi}_2\text{Te}_4$  can be viewed as a TI with intrinsic antiferromagnetic order due to an exchange field [15, 24, 54], which breaks time-reversal symmetry. In practice, the electric field can be applied by dual gate technology [35]. Without loss of generality, we assume that the electric field is applied along  $z$ -direction and can be described by an electric potential  $V_E$ , which is an odd function of  $z$ , i.e.,  $V_E(-z) = -V_E(z)$ . This corresponds to symmetric gating at top and bottom surfaces. Asymmetric gating affects our results quantitatively but not qualitatively.

We start from the bulk Hamiltonian of three-dimensional (3D) TIs and derive the four lowest-energy eigenstates at the  $\Gamma$  point as a basis [55–58]. Then, we project the antiferromagnetic order and the electric field into this basis. The resulting effective model for the  $\text{MnBi}_2\text{Te}_4$  thin films in presence of the electric field can be written as [59]

$$H = H_0 + H_{ex} + H_V, \quad (1)$$

where  $H_0$  describes the Dirac surface states of TIs given by

$$H_0 = h(\mathbf{k})\tau_z \otimes \sigma_z - \gamma\tau_0 \otimes (k_x\sigma_y - k_y\sigma_x) \quad (2)$$

with  $h(\mathbf{k}) = \Delta/2 - Bk^2$  and  $k^2 = k_x^2 + k_y^2$ .  $\tau_0$  and  $\sigma_0$  are  $2 \times 2$  identity matrices and  $\tau_i$  and  $\sigma_i$  with  $i = x, y, z$  are Pauli matrices acting on orbital and spin spaces, respectively.  $\Delta, B$  and  $\gamma$  are model parameters that depend on the thickness of the films [59]. For thick films, both  $\Delta$  and  $B$  approach zero.

The second term in Eq. (1), i.e.,  $H_{ex}$ , corresponds to the effective exchange field of the surface states. It opens a band gap in the spectrum of the Dirac surface states. Notably, the effective exchange field is different for even- and odd-layer thin films because of the antiferromagnetic order in the bulk. For even-layer films, the magnetization is compensated, whereas there is net magnetization for odd-layer films. As a result,  $H_{ex}$  reads

$$H_{ex}^{\text{odd}} = m_1\tau_0 \otimes \sigma_z \quad (3)$$

for odd-layer films, and

$$H_{ex}^{\text{even}} = m_2\tau_x \otimes \sigma_z \quad (4)$$

for even-layer films, where  $m_1$  and  $m_2$  are the corresponding strengths of the effective exchange field. The last

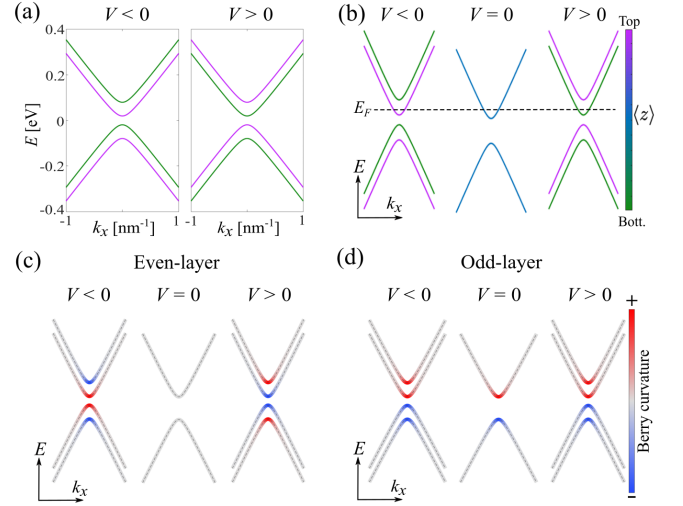


FIG. 2. (a) Spectra for antiferromagnetic  $\text{MnBi}_2\text{Te}_4$  films color-coded by the position expectation value  $\langle z \rangle$  along  $z$ -direction in presence of opposite electric field directions. (b) Spectra corresponding to case II in Fig. 1(a), color-coded by  $\langle z \rangle$ . The dashed line denotes the Fermi level at energy  $E_F$ . (c) Berry curvature distributions corresponding to case II in Fig. 1(a) for even-layer films. (d) The same as (c) but for odd-layer films. The chosen parameters are adopted to the material  $\text{MnBi}_2\text{Te}_4$  as described in the Supplemental Material [59].

term  $H_V$  in Eq. (1) stems from the electric field. It reflects the structure inversion asymmetry (SIA) of the two surfaces described by

$$H_V = V\tau_x \otimes \sigma_0 \quad (5)$$

with  $V$  being the SIA strength.

The SIA term  $H_V$  induced by external electric fields can shift top and bottom surface states relative to each other in energy due to the potential difference at opposite surfaces, illustrated by the color-coded position expectation value  $\langle z \rangle$  for the low-energy bands in Fig. 2(a). Reversing the direction of the electric field, this alters the shift pattern in an opposite way. Note that the shift patterns of the surface energy bands are the same in films with odd and even layers. This can be understood by recasting the effective model in the basis of top and bottom surfaces [59], i.e.,

$$h_s = sV + m_j s^{j-1} \sigma_z + \gamma(k_y \sigma_x - k_x \sigma_y), \quad (6)$$

where  $s = \pm$  denote top and bottom surfaces, respectively, and  $j = 1(2)$  indicates odd(even)-layer films. For simplicity, we assume in Eq. (6) that the films are thick enough such that the hybridization of top and bottom surface states can be ignored (i.e.,  $\Delta = 0$  and  $B = 0$ ). Evidently, the SIA strength  $V$  has opposite signs for top and bottom surface states. Hence, it shifts the Dirac bands in an opposite way. If the Fermi level is placed to

intersect the lowest conduction band, then flipping the direction of the external electric field (changing the sign of  $V$ ), this selects topological surface states from opposite surfaces.

Furthermore, the Berry curvature distributions of the surface states are strongly influenced by the SIA term  $H_V$ . For even-layer films, in the absence of an electric field ( $V = 0$ ), the Berry curvature of the lowest-energy band is zero [Fig. 2(c)] due to the presence of PT symmetry (i.e., combined space inversion and time-reversal symmetry) [33]. When the electric field is present ( $V \neq 0$ ), PT symmetry is broken. Hence, the degeneracy of the energy bands is lifted and the Berry curvature of each band becomes finite. In contrast, for odd-layer films, the Berry curvature is always non-zero due to the breaking of PT symmetry [19] no matter whether the electric field is present or not [Fig. 2(d)]. Moreover, the Berry curvature of the even-layer films is layer-locked for conduction (or valence) bands [35], illustrated in Figs. 2(a) and 2(c).

**Magnetic topological transistor.**— We now explain the working principle of the magnetic topological transistor, the two-terminal setup shown in Fig. 1(a). The two side regions of the junction under the influence of external electric fields are connected to source and drain of the transistor. The middle region is free of external fields. Exploiting the spatial dependence of the electric fields, the transistor can switch between “on” and “off” states depending on the relative direction of the electric fields, as illustrated in Fig. 1(b). When the electric fields are parallel, the transistor is in the “on” state with quantized conductance  $G \approx e^2/h$ . In contrast, when the electric fields are antiparallel, the transistor is in the “off” state with vanishing conductance  $G \approx 0$ .

The physics behind this transistor is the deterministic choice of conducting surface states at the Fermi level by external electric fields. At a given Fermi level, the top or bottom surface states can solely be responsible for transport since the electric field separates them in energy. Figure 2(b) sketches the low-energy spectra in three regions corresponding to case II of the transistor in Fig. 1(a). We set the direction of electric field on the left-hand side along  $+z$  such that the Fermi level only crosses the energy band of the top surface states. For the middle region of the transistor, the Fermi level crosses the energy bands of both top and bottom surface states. Eventually, the nature of the conducting surface states at the Fermi level on the right-hand side matters. If the top surface state on the right-hand side is responsible for transport [case I in Fig. 1(a)], then electrons traverse the junction easily and the conductance approaches  $G \approx e^2/h$ . Otherwise [case II in Fig. 1(a)], the conductance  $G$  approaches zero if the thickness of the middle region is large enough such that hybridization of top and bottom surface states is small.

**Numerical simulations.**— Up to now, we have analyzed the mechanism for our proposed magnetic topological

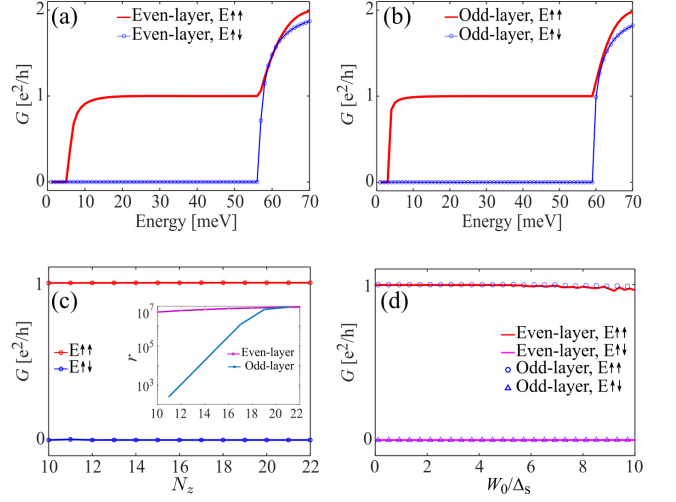


FIG. 3. (a) Conductance  $G$  of the magnetic topological transistor as a function of Fermi energy for different external field configurations. The symbols  $E\uparrow\uparrow$  and  $E\uparrow\downarrow$  represent the relative directions of the electric field for left and right leads to be parallel and antiparallel, respectively. We take  $N_z = 12$  (even layers). (b) The same as (a) but with  $N_z=13$  (odd layers). (c) Conductance  $G$  as a function of junction thickness  $N_z$  with  $E_F=30$  meV. The inset shows the on-off ratio  $r \equiv G_{\text{on}}/G_{\text{off}}$  as a function of  $N_z$ . Open (periodic) boundary conditions are imposed in  $z(y)$ -direction. (d) Conductance  $G$  as a function of disorder strength  $W_0/\Delta_s$  with  $N_z = 10, 11$ . The Fermi level is fixed at  $E_F=25$  meV. The other parameters in all plots are specified in [60].

transistor from a thick-film perspective. To directly analyze the performance of the transistor for any film thickness, we perform numerical calculations based on the discretized 3D bulk Hamiltonian on a cubic lattice [59], by employing the Landauer formalism [61–63]. We choose typical bulk parameters that are adopted to the material  $\text{MnBi}_2\text{Te}_4$  based on *ab initio* calculations [15]. The chosen sample geometry consists of a cuboidal central region and two semi-infinite leads as source and drain. Exploiting the recursive Green function technique [64], the conductance of the setup can be evaluated as

$$G = \frac{e^2}{h} \text{Tr}[\Gamma_L G^r \Gamma_R G^a], \quad (7)$$

where  $\Gamma_{L/R} = i(\Sigma_{L/R}^r - \Sigma_{L/R}^a)$  are the linewidth functions with  $\Sigma_{L/R}$  the self-energy due to the coupling to the left/right lead.  $G^r(G^a)$  is the retarded (advanced) Green function of the central region.

Figures 3(a) and 3(b) illustrate that the magnetic topological transistor works perfectly in a wide energy window, in which the conductance  $G$  approaches  $e^2/h$  for the “on” state (parallel configuration  $E\uparrow\uparrow$ ) and decrease to near zero for the “off” state (antiparallel configuration  $E\uparrow\downarrow$ ). This result is consistent with the phenomenological expectations discussed before. The on-off ratio

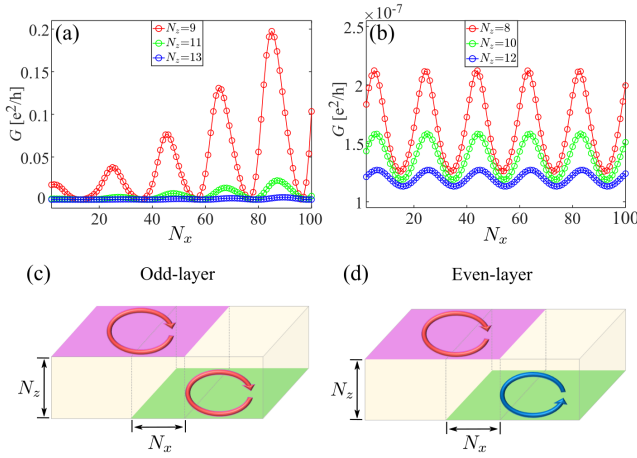


FIG. 4. (a) Conductance  $G$  as a function of  $N_x$  for case II in Fig. 1(a) with  $N_z = 9, 11$ , and  $13$ , respectively. (b) Conductance  $G$  as a function of  $N_x$  for case II in Fig. 1(a) with  $N_z = 8, 10$ , and  $12$ , respectively. We choose Fermi energy  $E_F = 30$  meV, and other parameters are the same as in Fig. 3. (c) Illustration of the Berry curvature for top surface (purple region) and bottom surface (green region) for antiparallel configuration  $E \uparrow \downarrow$  for odd-layer thin films. Red arrows and blue arrows represent opposite Berry curvature.  $N_x$  is the length of the middle region and  $N_z$  is the thickness of the thin films. (d) Illustration of the Berry curvature for top surface and bottom surface for antiparallel configuration  $E \uparrow \downarrow$  for even-layer thin films.

$r \equiv G_{\text{on}}/G_{\text{off}}$  of this transistor can reach  $10^7$  as shown in the inset of Fig. 3(c).

To obtain a large on-off ratio  $r$ , the thickness of the junction  $N_z$  should be large enough (i.e.,  $N_z \geq 10$ ) to avoid hybridization of top and bottom surface states, as shown in the inset of Fig. 3(c). The on-off ratio  $r$  increases as  $N_z$  grows. Odd-layer devices only perform well for thick films while even-layer devices are less sensitive to the film thickness. Moreover, to illustrate the robustness of the magnetic topological transistor against perturbations, Anderson-type disorder is introduced through random on-site potential with a uniform distribution within  $[-W_0/2, W_0/2]$ , where  $W_0$  denotes the disorder strength. It is evident from Fig. 3(d) that the proposed magnetic topological transistor persists to perform well in presence of disorder.

**Berry curvature features.**— For thick films, the hybridization of top and bottom surface states is negligible. However, as the film thickness decreases, the hybridization of top and bottom surfaces becomes pronounced. The tunneling of the surface electrons from top to bottom diminishes the functionality of the magnetic topological transistor. Figure 4(a) shows that the conductance  $G$  oscillates (as a function of  $N_x$ ) with larger and larger amplitudes as the thickness of the transistor  $N_z$  decreases in odd-layer thin films. In striking contrast, the conductance  $G$  of the even-layer thin films stays close to zero

(of the order of  $10^{-7} e^2/h$ ) even when  $N_z$  is quite small [Fig. 4(b)]. This difference can be attributed to the opposite Berry curvature of top and bottom surface states of even-layer system [Figs. 4(d) and 2(c)], in contrast to the same Berry curvature distribution of odd-layer system [Figs. 4(c) and 2(d)]. This finding implies that even-layer thin film devices are the better choice to build thin film transistors.

**Discussion and conclusion.**— Although our magnetic topological transistor is suggested explicitly for the antiferromagnetic TI  $\text{MnBi}_2\text{Te}_4$ , it can also be generalized to other magnetic TIs, for instance, ferromagnetic TIs doped with magnetic impurities [8, 59, 65–68]. It is worth noting that this type of transistor mechanism is absent in conventional TIs when the Dirac surface states are gapped by hybridization because top and bottom surface states can not be separated at the Fermi level in this case [59].

In summary, we have developed an effective model for the antiferromagnetic TI  $\text{MnBi}_2\text{Te}_4$  in presence of electric fields to demonstrate that electric fields can be exploited to selectively guide surface state transport. We have proposed a magnetic topological transistor based on three crucial ingredients: topology (for the emergence of surface states), exchange fields (to gap the surface states), and electric-field-induced structure inversion asymmetry (to shift the energy of top and bottom surface states). The proposed magnetic topological transistor is robust against disorder due to the topological nature of the surface states. It shows large on-off ratios when the magnetic TI films are thick enough to avoid hybridization. For thinner films, Berry curvature helps to improve the performance.

We thank Rui Chen for valuable discussions. This work was supported by the DFG (SPP1666 and SFB1170 “ToCoTronics”), the Würzburg-Dresden Cluster of Excellence ct.qmat, EXC2147, Project-id 390858490, and the Elitenetzwerk Bayern Graduate School on “Topological Insulators”. We thank the Bavarian Ministry of Economic Affairs, Regional Development and Energy for financial support within the High-Tech Agenda Project “Bausteine für das Quanten Computing auf Basis topologischer Materialien”. S.B.Z. acknowledges support by the European Research Council under the European Union’s Horizon 2020 research and innovation programme (ERC-StG-Neupert-757867-PARATOP) and from NCCR MARVEL funded by the SNSF. H.Z.L. acknowledges support by the National Natural Science Foundation of China (11925402).

\* haipeng.sun@physik.uni-wuerzburg.de

† changan.li@physik.uni-wuerzburg.de

[1] J. E. Moore, *Nature* **464**, 194 (2010).



- [2] M. Z. Hasan and C. L. Kane, *Rev. Mod. Phys.* **82**, 3045 (2010).
- [3] X.-L. Qi and S.-C. Zhang, *Rev. Mod. Phys.* **83**, 1057 (2011).
- [4] Q.-K. Xue, *Nat. Nanotechnol.* **6**, 197 (2011).
- [5] F. Xiu, L. He, Y. Wang, L. Cheng, L.-T. Chang, M. Lang, G. Huang, X. Kou, Y. Zhou, X. Jiang, Z. Chen, J. Zou, A. Shailos, and K. L. Wang, *Nat. Nanotechnol.* **6**, 216 (2011).
- [6] L. A. Wray, *Nat. Phys.* **8**, 705 (2012).
- [7] J. G. Checkelsky, J. Ye, Y. Onose, Y. Iwasa, and Y. Tokura, *Nat. Phys.* **8**, 729 (2012).
- [8] R. Yu, W. Zhang, H.-J. Zhang, S.-C. Zhang, X. Dai, and Z. Fang, *Science* **329**, 61 (2010).
- [9] P. Michetti and B. Trauzettel, *Appl. Phys. Lett.* **102**, 063503 (2013).
- [10] X. Qian, J. Liu, L. Fu, and J. Li, *Science* **346**, 1344 (2014).
- [11] J. Liu, T. H. Hsieh, P. Wei, W. Duan, J. Moodera, and L. Fu, *Nat. Mater.* **13**, 178 (2014).
- [12] J. Wang, B. Lian, and S.-C. Zhang, *Phys. Rev. Lett.* **115**, 036805 (2015).
- [13] Q. Liu, X. Zhang, L. B. Abdalla, A. Fazzio, and A. Zunger, *Nano Lett.* **15**, 1222 (2015).
- [14] J. L. Collins, A. Tadich, W. Wu, L. C. Gomes, J. N. B. Rodrigues, C. Liu, J. Hellerstedt, H. Ryu, S. Tang, S.-K. Mo, S. Adam, S. A. Yang, M. S. Fuhrer, and M. T. Edmonds, *Nature* **564**, 390 (2018).
- [15] D. Zhang, M. Shi, T. Zhu, D. Xing, H. Zhang, and J. Wang, *Phys. Rev. Lett.* **122**, 206401 (2019).
- [16] M. M. Otrokov, I. I. Klimovskikh, H. Bentmann, D. Estyunin, A. Zeugner, Z. S. Aliev, S. Gaß, A. U. B. Wolter, A. V. Koroleva, A. M. Shikin, M. Blanco-Rey, M. Hoffmann, I. P. Rusinov, A. Y. Vyazovskaya, S. V. Ereemeev, Y. M. Koroteev, V. M. Kuznetsov, F. Freyse, J. Sánchez-Barriga, I. R. Amiraslanov, M. B. Babanly, N. T. Mamedov, N. A. Abdullayev, V. N. Zverev, A. Alfonso, V. Kataev, B. Büchner, E. F. Schwier, S. Kumar, A. Kimura, L. Petaccia, G. Di Santo, R. C. Vidal, S. Schatz, R. K. Kießner, M. Ünzelmann, C. H. Min, S. Moser, T. R. F. Peixoto, F. Reinert, A. Ernst, P. M. Echenique, A. Isaeva, and E. V. Chulkov, *Nature* **576**, 416 (2019).
- [17] E. D. L. Rienks, S. Wimmer, J. Sánchez-Barriga, O. Caha, P. S. Mandal, J. Růžicka, A. Ney, H. Steiner, V. V. Volobuev, H. Groiss, M. Albu, G. Kothleitner, J. Michalička, S. A. Khan, J. Minár, H. Ebert, G. Bauer, F. Freyse, A. Varykhalov, O. Rader, and G. Springholz, *Nature* **576**, 423 (2019).
- [18] Y. Gong, J. Guo, J. Li, K. Zhu, M. Liao, X. Liu, Q. Zhang, L. Gu, L. Tang, X. Feng, D. Zhang, W. Li, C. Song, L. Wang, P. Yu, X. Chen, Y. Wang, H. Yao, W. Duan, Y. Xu, S.-C. Zhang, X. Ma, Q.-K. Xue, and K. He, *Chinese Phys. Lett.* **36**, 076801 (2019).
- [19] J. Li, Y. Li, S. Du, Z. Wang, B.-L. Gu, S.-C. Zhang, K. He, W. Duan, and Y. Xu, *Sci. Adv.* **5**, eaaw5685 (2019).
- [20] M. M. Otrokov, I. P. Rusinov, M. Blanco-Rey, M. Hoffmann, A. Y. Vyazovskaya, S. V. Ereemeev, A. Ernst, P. M. Echenique, A. Arnau, and E. V. Chulkov, *Phys. Rev. Lett.* **122**, 107202 (2019).
- [21] H. Sun, B. Xia, Z. Chen, Y. Zhang, P. Liu, Q. Yao, H. Tang, Y. Zhao, H. Xu, and Q. Liu, *Phys. Rev. Lett.* **123**, 096401 (2019).
- [22] C. Lei, S. Chen, and A. H. MacDonald, *Proceedings of the National Academy of Sciences* **117**, 27224 (2020).
- [23] H. Wang, D. Wang, Z. Yang, M. Shi, J. Ruan, D. Xing, J. Wang, and H. Zhang, *Phys. Rev. B* **101**, 081109 (2020).
- [24] R.-X. Zhang, F. Wu, and S. Das Sarma, *Phys. Rev. Lett.* **124**, 136407 (2020).
- [25] B. Lian, Z. Liu, Y. Zhang, and J. Wang, *Phys. Rev. Lett.* **124**, 126402 (2020).
- [26] C. Lei and A. H. MacDonald, *Phys. Rev. Materials* **5**, L051201 (2021).
- [27] B. Wei, J.-J. Zhu, Y. Song, and K. Chang, *Phys. Rev. B* **104**, 174436 (2021).
- [28] N. Varnava, J. H. Wilson, J. H. Pixley, and D. Vanderbilt, *Nat. Commun.* **12**, 3998 (2021).
- [29] M. Gu, J. Li, H. Sun, Y. Zhao, C. Liu, J. Liu, H. Lu, and Q. Liu, *Nat. Commun.* **12**, 3524 (2021).
- [30] H. Li, C.-Z. Chen, H. Jiang, and X. C. Xie, *Phys. Rev. Lett.* **127**, 236402 (2021).
- [31] R. Chen, S. Li, H.-P. Sun, Q. Liu, Y. Zhao, H.-Z. Lu, and X. C. Xie, *Phys. Rev. B* **103**, L241409 (2021).
- [32] W. Chen, Y. Zhao, Q. Yao, J. Zhang, and Q. Liu, *Phys. Rev. B* **103**, L201102 (2021).
- [33] S. Du, P. Tang, J. Li, Z. Lin, Y. Xu, W. Duan, and A. Rubio, *Phys. Rev. Research* **2**, 022025 (2020).
- [34] J. Cai, D. Ovchinnikov, Z. Fei, M. He, T. Song, Z. Lin, C. Wang, D. Cobden, J.-H. Chu, Y.-T. Cui, C.-Z. Chang, D. Xiao, J. Yan, and X. Xu, *Nat. Commun.* **13**, 1668 (2022).
- [35] A. Gao, Y.-F. Liu, C. Hu, J.-X. Qiu, C. Tzschaschel, B. Ghosh, S.-C. Ho, D. Bérubé, R. Chen, H. Sun, Z. Zhang, X.-Y. Zhang, Y.-X. Wang, N. Wang, Z. Huang, C. Felser, A. Agarwal, T. Ding, H.-J. Tien, A. Akey, J. Gardener, B. Singh, K. Watanabe, T. Taniguchi, K. S. Burch, D. C. Bell, B. B. Zhou, W. Gao, H.-Z. Lu, A. Bansil, H. Lin, T.-R. Chang, L. Fu, Q. Ma, N. Ni, and S.-Y. Xu, *Nature* **595**, 521 (2021).
- [36] C. Liu, Y. Wang, M. Yang, J. Mao, H. Li, Y. Li, J. Li, H. Zhu, J. Wang, L. Li, Y. Wu, Y. Xu, J. Zhang, and Y. Wang, *Nat. Commun.* **12**, 4647 (2021).
- [37] B. Chen, F. Fei, D. Zhang, B. Zhang, W. Liu, S. Zhang, P. Wang, B. Wei, Y. Zhang, Z. Zuo, J. Guo, Q. Liu, Z. Wang, X. Wu, J. Zong, X. Xie, W. Chen, Z. Sun, S. Wang, Y. Zhang, M. Zhang, X. Wang, F. Song, H. Zhang, D. Shen, and B. Wang, *Nat. Commun.* **10**, 4469 (2019).
- [38] Y.-J. Hao, P. Liu, Y. Feng, X.-M. Ma, E. F. Schwier, M. Arita, S. Kumar, C. Hu, R. Lu, M. Zeng, Y. Wang, Z. Hao, H.-Y. Sun, K. Zhang, J. Mei, N. Ni, L. Wu, K. Shimada, C. Chen, Q. Liu, and C. Liu, *Phys. Rev. X* **9**, 041038 (2019).
- [39] H. Li, S.-Y. Gao, S.-F. Duan, Y.-F. Xu, K.-J. Zhu, S.-J. Tian, J.-C. Gao, W.-H. Fan, Z.-C. Rao, J.-R. Huang, J.-J. Li, D.-Y. Yan, Z.-T. Liu, W.-L. Liu, Y.-B. Huang, Y.-L. Li, Y. Liu, G.-B. Zhang, P. Zhang, T. Kondo, S. Shin, H.-C. Lei, Y.-G. Shi, W.-T. Zhang, H.-M. Weng, T. Qian, and H. Ding, *Phys. Rev. X* **9**, 041039 (2019).
- [40] Y. J. Chen, L. X. Xu, J. H. Li, Y. W. Li, H. Y. Wang, C. F. Zhang, H. Li, Y. Wu, A. J. Liang, C. Chen, S. W. Jung, C. Cacho, Y. H. Mao, S. Liu, M. X. Wang, Y. F. Guo, Y. Xu, Z. K. Liu, L. X. Yang, and Y. L. Chen, *Phys. Rev. X* **9**, 041040 (2019).
- [41] P. Swatek, Y. Wu, L.-L. Wang, K. Lee, B. Schunk, J. Yan, and A. Kaminski, *Phys. Rev. B* **101**, 161109 (2020).

- [42] X. Wu, J. Li, X.-M. Ma, Y. Zhang, Y. Liu, C.-S. Zhou, J. Shao, Q. Wang, Y.-J. Hao, Y. Feng, E. F. Schwier, S. Kumar, H. Sun, P. Liu, K. Shimada, K. Miyamoto, T. Okuda, K. Wang, M. Xie, C. Chen, Q. Liu, C. Liu, and Y. Zhao, *Phys. Rev. X* **10**, 031013 (2020).
- [43] R. Lu, H. Sun, S. Kumar, Y. Wang, M. Gu, M. Zeng, Y.-J. Hao, J. Li, J. Shao, X.-M. Ma, Z. Hao, K. Zhang, W. Mansuer, J. Mei, Y. Zhao, C. Liu, K. Deng, W. Huang, B. Shen, K. Shimada, E. F. Schwier, C. Liu, Q. Liu, and C. Chen, *Phys. Rev. X* **11**, 011039 (2021).
- [44] R. C. Vidal, H. Bentmann, J. I. Facio, T. Heider, P. Kagerer, C. I. Fornari, T. R. F. Peixoto, T. Figge-meier, S. Jung, C. Cacho, B. Büchner, J. van den Brink, C. M. Schneider, L. Plucinski, E. F. Schwier, K. Shimada, M. Richter, A. Isaeva, and F. Reinert, *Phys. Rev. Lett.* **126**, 176403 (2021).
- [45] S. H. Lee, D. Graf, L. Min, Y. Zhu, H. Yi, S. Cio-cys, Y. Wang, E. S. Choi, R. Basnet, A. Fereidouni, A. Wegner, Y.-F. Zhao, K. Verlinde, J. He, R. Redwing, V. Gopalan, H. O. H. Churchill, A. Lanzara, N. Samarth, C.-Z. Chang, J. Hu, and Z. Q. Mao, *Phys. Rev. X* **11**, 031032 (2021).
- [46] M. Garnica, M. M. Otrokov, P. C. Aguilar, I. I. Klimovskikh, D. Estyunin, Z. S. Aliev, I. R. Amiraslanov, N. A. Abdullayev, V. N. Zverev, M. B. Babanly, N. T. Mamedov, A. M. Shikin, A. Arnau, A. L. V. de Parga, E. V. Chulkov, and R. Miranda, *npj Quantum Mater.* **7**, 1 (2022).
- [47] Y. Deng, Y. Yu, M. Z. Shi, Z. Guo, Z. Xu, J. Wang, X. H. Chen, and Y. Zhang, *Science* **367**, 895 (2020).
- [48] C. Liu, Y. Wang, H. Li, Y. Wu, Y. Li, J. Li, K. He, Y. Xu, J. Zhang, and Y. Wang, *Nat. Mater.* **19**, 522 (2020).
- [49] H. Deng, Z. Chen, A. Wołos, M. Konczykowski, K. Sobczak, J. Sitnicka, I. V. Fedorchenko, J. Borysiuk, T. Heider, L. Pluciński, K. Park, A. B. Georgescu, J. Cano, and L. Krusin-Elbaum, *Nat. Phys.* **17**, 36 (2021).
- [50] J. Ge, Y. Liu, J. Li, H. Li, T. Luo, Y. Wu, Y. Xu, and J. Wang, *Natl. Sci. Rev.* **7**, 1280 (2020).
- [51] D. Ovchinnikov, X. Huang, Z. Lin, Z. Fei, J. Cai, T. Song, M. He, Q. Jiang, C. Wang, H. Li, Y. Wang, Y. Wu, D. Xiao, J.-H. Chu, J. Yan, C.-Z. Chang, Y.-T. Cui, and X. Xu, *Nano Lett.* **21**, 2544 (2021).
- [52] J. Ge, Y. Liu, P. Wang, Z. Xu, J. Li, H. Li, Z. Yan, Y. Wu, Y. Xu, and J. Wang, *Phys. Rev. B* **105**, L201404 (2022).
- [53] A. Liang, C. Chen, H. Zheng, W. Xia, K. Huang, L. Wei, H. Yang, Y. Chen, X. Zhang, X. Xu, M. Wang, Y. Guo, L. Yang, Z. Liu, and Y. Chen, *Nano Lett.* [10.1021/acs.nanolett.1c04930](https://doi.org/10.1021/acs.nanolett.1c04930) (2022).
- [54] H. Zhang, C.-X. Liu, X.-L. Qi, X. Dai, Z. Fang, and S.-C. Zhang, *Nat. Phys.* **5**, 438 (2009).
- [55] H.-P. Sun, C. M. Wang, S.-B. Zhang, R. Chen, Y. Zhao, C. Liu, Q. Liu, C. Chen, H.-Z. Lu, and X. C. Xie, *Phys. Rev. B* **102**, 241406 (2020).
- [56] H.-Z. Lu, A. Zhao, and S.-Q. Shen, *Phys. Rev. Lett.* **111**, 146802 (2013).
- [57] W.-Y. Shan, H.-Z. Lu, and S.-Q. Shen, *New J. Phys.* **12**, 043048 (2010).
- [58] H.-Z. Lu, W.-Y. Shan, W. Yao, Q. Niu, and S.-Q. Shen, *Phys. Rev. B* **81**, 115407 (2010).
- [59] See Supplemental Material for more details. The Supplemental Material includes four parts: (i) the derivation of the effective model for surface states, (ii) lattice model for magnetic TIs in presence of electric fields, (iii) transport results for ferromagnetic TIs, and (iv) transport results for 3D TIs.
- [60] Numerical transport calculations are based on the discretized 3D bulk Hamiltonian on a cubic lattice explicitly explained in the Supplemental Material. The bulk parameters are adopted to the material  $\text{MnBi}_2\text{Te}_4$  as  $A_1=270.23$  meV·nm,  $A_2=319.64$  meV·nm,  $B_1=119.05$  meV·nm<sup>2</sup>,  $B_2=94.05$  meV·nm<sup>2</sup>,  $M_0=-116.50$  meV,  $m=50$  meV. Here, we choose the parameter  $V_z = 5$  meV in Fig. 3(a,b,d) and Fig. 4(a,b), and  $V_z = 3$  meV in Fig. 3(c).  $\Delta_s$  in Fig. 3(d) is the surface energy gap used to measure the strength of the on-site disorder.
- [61] R. Landauer, *The Philosophical Magazine* **21**, 863 (1970).
- [62] M. Büttiker, *Phys. Rev. Lett.* **57**, 1761 (1986).
- [63] S. Datta, *Electronic Transport in Mesoscopic Systems* (Cambridge University Press, 1997).
- [64] A. MacKinnon, *Z. Physik B - Condensed Matter* **59**, 385 (1985).
- [65] J. Henk, M. Flieger, I. V. Maznichenko, I. Mertig, A. Ernst, S. V. Eremeev, and E. V. Chulkov, *Phys. Rev. Lett.* **109**, 076801 (2012).
- [66] C.-Z. Chang, J. Zhang, X. Feng, J. Shen, Z. Zhang, M. Guo, K. Li, Y. Ou, P. Wei, L.-L. Wang, Z.-Q. Ji, Y. Feng, S. Ji, X. Chen, J. Jia, X. Dai, Z. Fang, S.-C. Zhang, K. He, Y. Wang, L. Lu, X.-C. Ma, and Q.-K. Xue, *Science* **340**, 167 (2013).
- [67] C.-Z. Chang, W. Zhao, D. Y. Kim, H. Zhang, B. A. Assaf, D. Heiman, S.-C. Zhang, C. Liu, M. H. W. Chan, and J. S. Moodera, *Nat. Mater.* **14**, 473 (2015).
- [68] M. Mogi, R. Yoshimi, A. Tsukazaki, K. Yasuda, Y. Kozuka, K. S. Takahashi, M. Kawasaki, and Y. Tokura, *Appl. Phys. Lett.* **107**, 182401 (2015).

# Supplemental Material for “Magnetic Topological Transistor”

Hai-Peng Sun,<sup>1,\*</sup> Chang-An Li,<sup>1,†</sup> Song-Bo Zhang,<sup>2</sup> Hai-Zhou Lu,<sup>3,4</sup> and Björn Trauzettel<sup>1,5</sup>

<sup>1</sup>*Institute for Theoretical Physics and Astrophysics,  
University of Würzburg, 97074 Würzburg, Germany*

<sup>2</sup>*Department of Physics, University of Zürich, Winterthurerstrasse 190, 8057, Zürich, Switzerland*

<sup>3</sup>*Shenzhen Institute for Quantum Science and Engineering and Department of Physics,  
Southern University of Science and Technology (SUSTech), Shenzhen, 518055, China*

<sup>4</sup>*Shenzhen Key Laboratory of Quantum Science and Engineering, Shenzhen, 518055, China*

<sup>5</sup>*Würzburg-Dresden Cluster of Excellence ct.qmat, Germany*

(Dated: June 23, 2022)

In the following, we discuss the derivation of the effective model of surface states for antiferromagnetic topological insulator (TI)  $\text{MnBi}_2\text{Te}_4$  in presence of an electric field. We also present the lattice model for the antiferromagnetic TI  $\text{MnBi}_2\text{Te}_4$  and the counterpart for ferromagnetic TIs. They are used for numerical calculations of transport properties. Finally, we discuss transport results of ferromagnetic TIs and 3D TIs and compare them to the ones shown in the main text for antiferromagnetic TIs.

## CONTENTS

SI. Effective model for surface states	S1
A. 3D bulk Hamiltonian for antiferromagnetic $\text{MnBi}_2\text{Te}_4$ in presence of an electric field	S1
B. Wave functions and eigen energies for $\text{MnBi}_2\text{Te}_4$ thin films	S2
C. Effective model for $\text{MnBi}_2\text{Te}_4$ thin films in presence of an electric field	S2
D. $\text{MnBi}_2\text{Te}_4$ thick films	S4
SII. Lattice model for magnetic TIs in presence of electric fields	S4
SIII. Transport results for ferromagnetic TIs	S5
SIV. Transport results for 3D TIs	S5
References	S5

## SI. EFFECTIVE MODEL FOR SURFACE STATES

### A. 3D bulk Hamiltonian for antiferromagnetic $\text{MnBi}_2\text{Te}_4$ in presence of an electric field

The 3D bulk Hamiltonian in presence of an external electric field for antiferromagnetic  $\text{MnBi}_2\text{Te}_4$  reads

$$\mathcal{H}(\mathbf{k}) = \mathcal{H}_N(\mathbf{k}) + \mathcal{H}_X(z) + V_E(z), \quad (\text{S1})$$

where  $\mathcal{H}_N(\mathbf{k})$  is the non-magnetic part,  $\mathcal{H}_X(z)$  is the exchange field that accounts for the out-of-plane antiferromagnetic order, and  $V_E(z)$  is the electric potential induced by the external electric field. The non-magnetic part is given by

$$\mathcal{H}_N(\mathbf{k}) = \epsilon_0(\mathbf{k}) + \begin{bmatrix} M(\mathbf{k}) & A_1 k_z & 0 & A_2 k_- \\ A_1 k_z & -M(\mathbf{k}) & A_2 k_- & 0 \\ 0 & A_2 k_+ & M(\mathbf{k}) & -A_1 k_z \\ A_2 k_+ & 0 & -A_1 k_z & -M(\mathbf{k}) \end{bmatrix} \quad (\text{S2})$$

with  $k_{\pm} = k_x \pm ik_y$ ,  $\epsilon_0(\mathbf{k}) = C_0 + D_1 k_z^2 + D_2(k_x^2 + k_y^2)$  and  $M(\mathbf{k}) = M_0 - B_1 k_z^2 - B_2(k_x^2 + k_y^2)$ .  $C_0$ ,  $D_i$ ,  $M_0$ ,  $B_i$  and  $A_i$  are model parameters with  $i = 1, 2$ . The basis of the Hamiltonian is  $\{|P1_z^+, \uparrow\rangle, |P2_z^-, \uparrow\rangle, |P1_z^+, \downarrow\rangle, |P2_z^-, \downarrow\rangle\}$ .

The exchange field reads

$$\mathcal{H}_X(z) = m_z(z) \sigma_z \otimes \tau_0, \quad (\text{S3})$$

where  $m_z(z) = -m_0 \sin(\pi z/d)$  is the magnetization energy along  $z$ -direction with  $m_0$  the amplitude of the intralayer ferromagnetic order,  $d$  is the thickness of a septuple layer,  $\sigma_z$  is the Pauli  $z$  matrix for spin degrees of freedom, and  $\tau_0$  is a  $2 \times 2$  identity matrix for orbital degrees of freedom.

We assume the electric potential  $V_E(z)$  is an odd function of  $z$ , namely,  $V_E(-z) = -V_E(z)$ , which corresponds to symmetric gating. The qualitative findings of ours are not affected by this choice.

### B. Wave functions and eigen energies for MnBi<sub>2</sub>Te<sub>4</sub> thin films

Consider a MnBi<sub>2</sub>Te<sub>4</sub> thin film with thickness  $L$  along  $z$ -direction and label bottom and top boundaries as  $-L/2$  and  $L/2$ , respectively. First, we derive the surface eigenstates of the non-magnetic part at the  $\Gamma$  point ( $k_x = k_y = 0$ ), which form the basis for the effective model. Replacing  $k_z$  by  $-i\partial_z$ , since  $k_z$  is no longer a good quantum number, and taking  $k_x = k_y = 0$  in  $\mathcal{H}_N(\mathbf{k})$ , we arrive at  $\mathcal{H}_N(-i\partial_z)$ , where

$$\mathcal{H}_N(-i\partial_z) = \begin{bmatrix} h_N(A_1) & 0 \\ 0 & h_N(-A_1) \end{bmatrix}. \quad (\text{S4})$$

with  $h_N(A_1) = C - D_1\partial_z^2 + (M + B_1\partial_z^2)\sigma_z - iA_1\partial_z\sigma_x$ . The general eigenstate for  $h_N(A_1)$  reads

$$\psi(z) = C_{\alpha,\beta} \psi_{\alpha,\beta} e^{\beta\lambda_\alpha z}, \quad (\text{S5})$$

where

$$\psi_{\alpha,\beta} = \begin{bmatrix} -D_+\lambda_\alpha^2 + l_- - E \\ iA_1\beta\lambda_\alpha \end{bmatrix}, \quad \lambda_\alpha = \sqrt{\frac{-F + (-1)^{\alpha-1}\sqrt{R}}{2(D_1^2 - B_1^2)}} \quad (\text{S6})$$

with  $\alpha = 1, 2$ ,  $\beta = \pm$ ,  $D_+ = D_1 + B_1$ ,  $l_- = C_0 - M_0$ ,  $F = A_1^2 - 2B_1M_0 + 2D_1(E_0 - C_0)$ , and  $R = F^2 - 4(D_1^2 - B_1^2)(E - C_0 - M_0)(E - C_0 + M_0)$ .

Using open boundary conditions at  $z = \pm L/2$ , namely,  $\psi(\pm L/2) = 0$ , we obtain the transcendental equations for the eigenenergies

$$E_+ = \frac{(-D_+\lambda_1^2 + l_-)\lambda_2 \tanh(\lambda_1 L/2) - (-D_+\lambda_2^2 + l_-)\lambda_1 \tanh(\lambda_2 L/2)}{\lambda_2 \tanh(\lambda_1 L/2) - \lambda_1 \tanh(\lambda_2 L/2)}, \quad (\text{S7})$$

$$E_- = \frac{(-D_+\lambda_1^2 + l_-)\lambda_2 \tanh(\lambda_2 L/2) - (-D_+\lambda_2^2 + l_-)\lambda_1 \tanh(\lambda_1 L/2)}{\lambda_2 \tanh(\lambda_2 L/2) - \lambda_1 \tanh(\lambda_1 L/2)}. \quad (\text{S8})$$

Moreover, we find the wave functions from the general solution as

$$\varphi(A_1) = C_+ \begin{bmatrix} -D_+ f_+^+(z) \eta^+ \\ iA_1 f_+^+(z) \end{bmatrix}, \quad \chi(A_1) = C_- \begin{bmatrix} -D_+ f_+^-(z) \eta^- \\ iA_1 f_+^-(z) \end{bmatrix} \quad (\text{S9})$$

with

$$f_+^\pm(z) = \frac{\cosh(\lambda_1 z)}{\cosh(\lambda_1 \frac{L}{2})} - \frac{\cosh(\lambda_2 z)}{\cosh(\lambda_2 \frac{L}{2})} \Big|_{E=E_\pm}, \quad f_-^\pm(z) = \frac{\sinh(\lambda_1 z)}{\sinh(\lambda_1 \frac{L}{2})} - \frac{\sinh(\lambda_2 z)}{\sinh(\lambda_2 \frac{L}{2})} \Big|_{E=E_\pm}, \quad (\text{S10})$$

$$\eta^+ = \frac{\lambda_2^2 - \lambda_1^2}{\lambda_2 \coth(\lambda_2 \frac{L}{2}) - \lambda_1 \coth(\lambda_1 \frac{L}{2})} \Big|_{E=E_+}, \quad \eta^- = \frac{\lambda_2^2 - \lambda_1^2}{\lambda_2 \tanh(\lambda_2 \frac{L}{2}) - \lambda_1 \tanh(\lambda_1 \frac{L}{2})} \Big|_{E=E_-}. \quad (\text{S11})$$

The normalization coefficients  $C_+$  and  $C_-$  are given by

$$1/|C_+|^2 = \int_{-\frac{L}{2}}^{\frac{L}{2}} dz [D_+^2 |f_+^-(z) \eta^+|^2 + A_1^2 |f_+^+(z)|^2], \quad 1/|C_-|^2 = \int_{-\frac{L}{2}}^{\frac{L}{2}} dz [D_+^2 |f_+^-(z) \eta^-|^2 + A_1^2 |f_+^-(z)|^2]. \quad (\text{S12})$$

Thus, the wave functions for  $\mathcal{H}_N(-i\partial_z)$  reads

$$\Phi_1 = \begin{bmatrix} \varphi(A_1) \\ 0 \end{bmatrix}, \quad \Phi_2 = \begin{bmatrix} \chi(A_1) \\ 0 \end{bmatrix}, \quad \Phi_3 = \begin{bmatrix} 0 \\ \varphi(-A_1) \end{bmatrix}, \quad \Phi_4 = \begin{bmatrix} 0 \\ \chi(-A_1) \end{bmatrix}, \quad (\text{S13})$$

### C. Effective model for MnBi<sub>2</sub>Te<sub>4</sub> thin films in presence of an electric field

Projecting the 3D bulk Hamiltonian for MnBi<sub>2</sub>Te<sub>4</sub> to the basis  $\{\Phi_1, \Phi_4, \Phi_2, \Phi_3\}$ , we obtain the effective model as

$$H = \int_{-\frac{L}{2}}^{\frac{L}{2}} dz [\Phi_1, \Phi_4, \Phi_2, \Phi_3]^\dagger \mathcal{H}(\mathbf{k}) [\Phi_1, \Phi_4, \Phi_2, \Phi_3] \quad (\text{S14})$$

$$= \int_{-\frac{L}{2}}^{\frac{L}{2}} dz [\Phi_1, \Phi_4, \Phi_2, \Phi_3]^\dagger [\mathcal{H}_N(\mathbf{k}) + \mathcal{H}_X(z) + V_E(z)] [\Phi_1, \Phi_4, \Phi_2, \Phi_3] \quad (\text{S15})$$

$$= H_0 + H_{ex} + H_V, \quad (\text{S16})$$



where

$$H_0 = \int_{-\frac{L}{2}}^{\frac{L}{2}} dz [\Phi_1, \Phi_4, \Phi_2, \Phi_3]^\dagger \mathcal{H}_N(\mathbf{k}) [\Phi_1, \Phi_4, \Phi_2, \Phi_3] \quad (\text{S17})$$

$$= E_0 - Dk^2 + \begin{bmatrix} \frac{\Delta}{2} - Bk^2 & \tilde{A}_2 k_- & 0 & 0 \\ \tilde{A}_2^* k_+ & -\frac{\Delta}{2} + Bk^2 & 0 & 0 \\ 0 & 0 & -\frac{\Delta}{2} + Bk^2 & -\tilde{A}_2^* k_- \\ 0 & 0 & -\tilde{A}_2 k_+ & \frac{\Delta}{2} - Bk^2 \end{bmatrix}, \quad (\text{S18})$$

with  $E_0 = (E_+ + E_-)/2$ ,  $\Delta = E_+ - E_-$ ,  $B = (\tilde{B}_1 - \tilde{B}_2)/2$ ,  $D = (\tilde{B}_1 + \tilde{B}_2)/2 - D_2$ ,  $\tilde{B}_1 = B_2 \langle \varphi(A_1) | \sigma_z | \varphi(A_1) \rangle$ ,  $\tilde{B}_2 = B_2 \langle \chi(A_1) | \sigma_z | \chi(A_1) \rangle$ , and  $\tilde{A}_2 = A_2 \langle \varphi(A_1) | \sigma_x | \chi(-A_1) \rangle$ .

For simplicity, we ignore the energy shift  $E_0$  and the particle-hole asymmetry term  $Dk^2$  in the following, which implies that  $\epsilon_0(\mathbf{k}) = 0$ . Thus,

$$H_0 = h(k) \tau_z \otimes \sigma_z - \gamma \tau_0 \otimes (k_x \sigma_y - k_y \sigma_x), \quad (\text{S19})$$

where  $h(k) = \Delta/2 - Bk^2$ ,  $k^2 = k_x^2 + k_y^2$ , and  $\gamma = -i\tilde{A}_2$ .

The effective exchange field  $H_{ex}(z)$  for odd-layer thin films reads

$$H_{ex}^{\text{odd}} = \int_{-\frac{L}{2}}^{\frac{L}{2}} dz [\Phi_1, \Phi_4, \Phi_2, \Phi_3]^\dagger \mathcal{H}_X(z) [\Phi_1, \Phi_4, \Phi_2, \Phi_3] = m_1 \tau_0 \otimes \sigma_z, \quad (\text{S20})$$

where  $m_1 = (-1)^{\frac{N_z-1}{2}} m_0 \langle \varphi(A_1) | \cos(\frac{\pi}{d} z) \sigma_0 | \varphi(A_1) \rangle$  with  $N_z$  the number of layers.

The effective exchange field  $H_{ex}(z)$  for even-layer thin films reads

$$H_{ex}^{\text{even}} = \int_{-\frac{L}{2}}^{\frac{L}{2}} dz [\Phi_1, \Phi_4, \Phi_2, \Phi_3]^\dagger \mathcal{H}_X(z) [\Phi_1, \Phi_4, \Phi_2, \Phi_3] = m_2 \tau_x \otimes \sigma_z, \quad (\text{S21})$$

where  $m_2 = (-1)^{\frac{N_z}{2}-1} m_0 \langle \varphi(A_1) | \sin(\frac{\pi}{d} z) \sigma_0 | \chi(A_1) \rangle$  with  $N_z$  the number of layers. In Eqs.(S20) and (S21),  $m_1$  and  $m_2$  are the strengths of the effective exchange field for the surface states of odd- and even-layer thin films, respectively.  $H_{ex}^{\text{odd}}$  and  $H_{ex}^{\text{even}}$  are not the same because of the different profiles of bulk magnetization.

Structure inversion asymmetry (SIA) induced by the electric field is described by

$$H_V = \int_{-\frac{L}{2}}^{\frac{L}{2}} dz [\Phi_1, \Phi_4, \Phi_2, \Phi_3]^\dagger V_E(z) [\Phi_1, \Phi_4, \Phi_2, \Phi_3] = V \tau_x \otimes \sigma_0, \quad (\text{S22})$$

where  $V = \langle \varphi(A_1) | V_E(z) \sigma_0 | \chi(A_1) \rangle$  is the strength of SIA.

In summary, the effective model for odd-layer  $\text{MnBi}_2\text{Te}_4$  thin films in presence of electric fields reads

$$H_{\text{odd}} = \begin{bmatrix} h(k) + m_1 & i\gamma k_- & V & 0 \\ -i\gamma k_+ & -h(k) - m_1 & 0 & V \\ V & 0 & -h(k) + m_1 & i\gamma k_- \\ 0 & V & -i\gamma k_+ & h(k) - m_1 \end{bmatrix}, \quad (\text{S23})$$

where  $h(k) = \Delta/2 - Bk^2$ ,  $k^2 = k_x^2 + k_y^2$ .

Likewise, the effective model for even-layer  $\text{MnBi}_2\text{Te}_4$  thin films reads

$$H_{\text{even}} = \begin{bmatrix} h(k) & i\gamma k_- & V + m_2 & 0 \\ -i\gamma k_+ & -h(k) & 0 & V - m_2 \\ V + m_2 & 0 & -h(k) & i\gamma k_- \\ 0 & V - m_2 & -i\gamma k_+ & h(k) \end{bmatrix}. \quad (\text{S24})$$

The parameters of the effective model for antiferromagnetic  $\text{MnBi}_2\text{Te}_4$  thin films used in Fig. 2 are shown below. Note that the parameters for the effective model are obtained from the bulk parameters extracted from *ab initio* calculations [1].

TABLE S1. Parameters of the effective model for antiferromagnetic MnBi<sub>2</sub>Te<sub>4</sub> thin films with different typical  $N_z$  (the number of septuple layers).

$N_z$	$\Delta$	$B$	$\gamma$	$m_1$	$m_2$	$V$
10	-0.34 meV	1.31 meV·nm <sup>2</sup>	319.64 meV·nm	0 meV	35.02 meV	20 meV
11	-0.16 meV	0.67 meV·nm <sup>2</sup>	319.64 meV·nm	35.02 meV	0 meV	20 meV

#### D. MnBi<sub>2</sub>Te<sub>4</sub> thick films

For MnBi<sub>2</sub>Te<sub>4</sub> thick films, the parameters  $\Delta$  and  $B$  approach zero, which implies that  $h(k) = 0$ . Therefore, the effective model for odd-layer MnBi<sub>2</sub>Te<sub>4</sub> thick films in presence of electric fields reads

$$H_{\text{odd}} = \begin{bmatrix} m_1 & i\gamma k_- & V & 0 \\ -i\gamma k_+ & -m_1 & 0 & V \\ V & 0 & m_1 & i\gamma k_- \\ 0 & V & -i\gamma k_+ & -m_1 \end{bmatrix}. \quad (\text{S25})$$

We block-diagonalize this effective model via a unitary transformation

$$U_1^\dagger H_{\text{odd}} U_1 = \begin{bmatrix} V + m_1 & i\gamma k_- & 0 & 0 \\ -i\gamma k_+ & V - m_1 & 0 & 0 \\ 0 & 0 & -V + m_1 & i\gamma k_- \\ 0 & 0 & -i\gamma k_+ & -V - m_1 \end{bmatrix}, \quad (\text{S26})$$

where

$$U_1 = \frac{1}{\sqrt{2}} \begin{bmatrix} 1 & 0 & -1 & 0 \\ 0 & 1 & 0 & -1 \\ 1 & 0 & 1 & 0 \\ 0 & 1 & 0 & 1 \end{bmatrix}. \quad (\text{S27})$$

Similarly, the effective model for even-layer MnBi<sub>2</sub>Te<sub>4</sub> thick films reads

$$H_{\text{even}} = \begin{bmatrix} 0 & i\gamma k_- & V + m_2 & 0 \\ -i\gamma k_+ & 0 & 0 & V - m_2 \\ V + m_2 & 0 & 0 & i\gamma k_- \\ 0 & V - m_2 & -i\gamma k_+ & 0 \end{bmatrix}. \quad (\text{S28})$$

Again, we block-diagonalize this effective model through unitary transformation

$$U_2^\dagger H_{\text{even}} U_2 = \begin{bmatrix} V + m_2 & i\gamma k_- & 0 & 0 \\ -i\gamma k_+ & V - m_2 & 0 & 0 \\ 0 & 0 & -V - m_2 & i\gamma k_- \\ 0 & 0 & -i\gamma k_+ & -V + m_2 \end{bmatrix}, \quad (\text{S29})$$

where

$$U_2 = \frac{1}{\sqrt{2}} \begin{bmatrix} 1 & 0 & -1 & 0 \\ 0 & 1 & 0 & -1 \\ 1 & 0 & 1 & 0 \\ 0 & 1 & 0 & 1 \end{bmatrix}. \quad (\text{S30})$$

### SIII. LATTICE MODEL FOR MAGNETIC TIS IN PRESENCE OF ELECTRIC FIELDS

The bulk Hamiltonian of Eq.(S1) can be regularized on a cubic lattice by the substitutions  $k_j \rightarrow \frac{1}{a_0} \sin(k_j a_0)$ ,  $k_j^2 \rightarrow \frac{2}{a_0^2} [1 - \cos(k_j a_0)]$ , where  $a_0$  is the lattice constant and  $j = x, y, z$ . For simplicity, we take  $a_0 = 1$  nm. The three lattice translation vectors are defined as  $a_1 = (1, 0, 0)^T$ ,  $a_2 = (0, 1, 0)^T$ ,  $a_3 = (0, 0, 1)^T$ . The lattice model for antiferromagnetic MnBi<sub>2</sub>Te<sub>4</sub> reads

$$H(\mathbf{k}) = H_0(\mathbf{k}) + H_{ex} + V_E, \quad (\text{S31})$$

where

$$H_0(\mathbf{k}) = \sum_0^3 d_i(\mathbf{k}) \Gamma_i \quad (\text{S32})$$

with  $\Gamma_i = \sigma_i \otimes \tau_1$  for  $i = 1, 2, 3$ , and  $\Gamma_0 = \sigma_0 \otimes \tau_3$ .  $\sigma_i$  and  $\tau_i$  are Pauli matrices for the spin and orbital degrees of freedom, respectively,  $d_0 = M_0 + 2B_1 [1 - \cos(k_z)] + 2B_2 [2 - \cos(k_x) - \cos(k_y)]$ ,  $d_1 = A_2 \sin(k_x)$ ,  $d_2 = A_2 \sin(k_y)$ ,

and  $d_3 = A_1 \sin(k_z)$ . The exchange field reads

$$H_{ex} = \begin{bmatrix} \vec{M}_A \cdot \vec{\sigma} \otimes \tau_0 & 0 \\ 0 & \vec{M}_B \cdot \vec{\sigma} \otimes \tau_0 \end{bmatrix}. \quad (\text{S33})$$

For the antiferromagnetic  $\text{MnBi}_2\text{Te}_4$ , we introduce a sublayer index  $i = A, B$  to describe the unit-cell doubling and characterize the magnetization in sublayer  $i$  by  $M_i = m(\cos \phi_i \sin \theta_i, \sin \phi_i \sin \theta_i, \cos \theta_i)$  with angles  $\phi_i$  and  $\theta_i$ . The A-type antiferromagnetic order is described by  $(\theta_A, \theta_B) = (0, \pi)$  and  $(\phi_A, \phi_B) = (0, 0)$ , where

$$H_{ex} = \begin{bmatrix} m \sigma_z \otimes \tau_0 & 0 \\ 0 & -m \sigma_z \otimes \tau_0 \end{bmatrix}. \quad (\text{S34})$$

The electric potential is  $V_E = V(z) \sigma_0 \otimes \tau_0$ , where  $V(z)$  depicts the strength of the electric field. In the lattice model, the electric potential difference of neighbouring layers is  $V_z$ .

Notably, the lattice model for the ferromagnetic case is the same as that for the antiferromagnetic case except for the exchange field part, where  $H_{ex}^{FM} = m \sigma_z \otimes \tau_0$ .

### SIII. TRANSPORT RESULTS FOR FERROMAGNETIC TIS

Our proposal is based on gapped surface states. This indicates that such magnetic topological transistors can also be built based on a ferromagnetic TI. For a ferromagnetic TI, the magnetization first opens a band gap at the Dirac point due to the breaking of the time-reversal symmetry. In this case, SIA pushes the top and bottom Dirac bands to opposite directions in energy as shown in Fig. S1(a). Thus, only top or bottom surface states are selected when the Fermi level is placed within lowest conduction band. Consequently, the magnetic topological transistor can be made of a ferromagnetic TI, as verified by the numerical results in Fig. S1(c). The ferromagnetic topological transistor has the same performance as the antiferromagnetic case for thick films. But its performance is worse for the ultra-thin film devices due to the same Berry curvature of top and bottom surface states at the Fermi level, which is similar to the case of odd-layer  $\text{MnBi}_2\text{Te}_4$ .

### SIV. TRANSPORT RESULTS FOR 3D TIS

For a 3D TI, the Dirac surface states are degenerate due to time-reversal symmetry. When SIA is present, top and bottom Dirac cones are shifted towards opposite directions in energy. For a thin film made of 3D TIs, top and bottom surface states hybridize, which opens an energy gap as shown in Fig. S1 (b). Consider the same setup as in Fig. 1(a) but made of TI thin films. The topological transistor does not function because of the unavoidable simultaneous crossing of top and bottom surface states by the Fermi level. It is clear from Fig. S1(d) that the conductance can not distinguish two different electric field configurations.

---

\* [haipeng.sun@physik.uni-wuerzburg.de](mailto:haipeng.sun@physik.uni-wuerzburg.de)

† [changan.li@physik.uni-wuerzburg.de](mailto:changan.li@physik.uni-wuerzburg.de)

- [1] D. Zhang, M. Shi, T. Zhu, D. Xing, H. Zhang, and J. Wang, *Phys. Rev. Lett.* **122**, 206401 (2019).
- [2] H. Zhang, C.-X. Liu, X.-L. Qi, X. Dai, Z. Fang, and S.-C. Zhang, *Nat. Phys.* **5**, 438 (2009).
- [3] C.-Z. Chang, J. Zhang, X. Feng, J. Shen, Z. Zhang, M. Guo, K. Li, Y. Ou, P. Wei, L.-L. Wang, Z.-Q. Ji, Y. Feng, S. Ji, X. Chen, J. Jia, X. Dai, Z. Fang, S.-C. Zhang, K. He, Y. Wang, L. Lu, X.-C. Ma, and Q.-K. Xue, *Science* **340**, 167 (2013).
- [4] C.-Z. Chang, W. Zhao, D. Y. Kim, H. Zhang, B. A. Assaf, D. Heiman, S.-C. Zhang, C. Liu, M. H. W. Chan, and J. S. Moodera, *Nat. Mater.* **14**, 473 (2015).
- [5] M. Mogi, R. Yoshimi, A. Tsukazaki, K. Yasuda, Y. Kozuka, K. S. Takahashi, M. Kawasaki, and Y. Tokura, *Appl. Phys. Lett.* **107**, 182401 (2015).

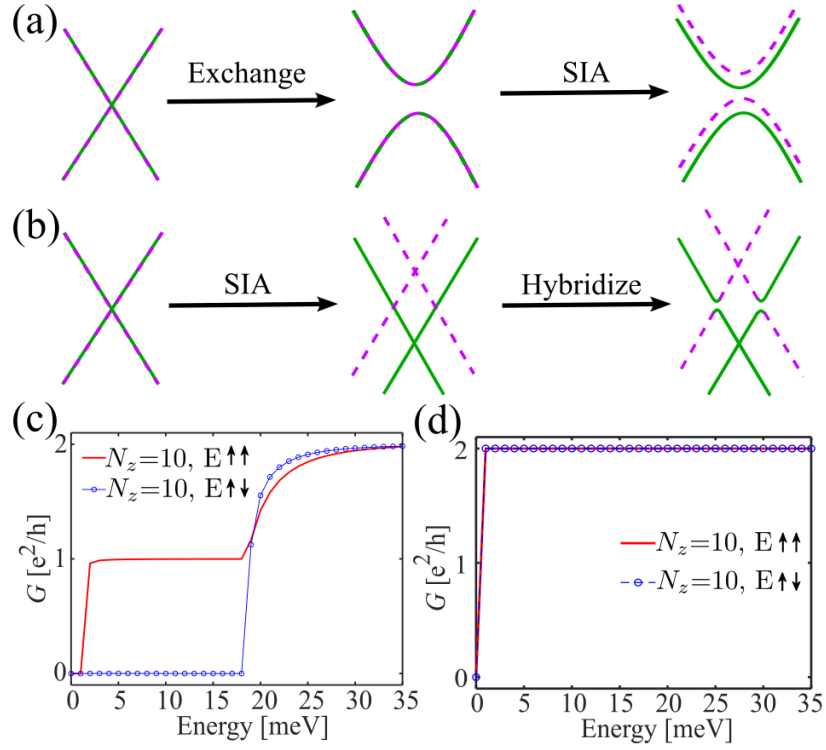


FIG. S1. (a) Schematic of the band structure of topological Dirac surface states under the influence of exchange field and SIA. There is a competition between magnetization and SIA as magnetization opens a band gap while SIA shrinks the band gap. Dashed purple lines and solid green lines represent the Dirac cones at top and bottom surfaces, respectively. (b) Schematic of the band structure of topological Dirac surface states under the influence of SIA and hybridization. (c) Conductance  $G$  as a function of Fermi energy for a ferromagnetic TI with  $N_z=10$ ,  $V_z=2$  meV and  $m=10$  meV. (d) Conductance  $G$  as a function of Fermi energy for a TI with  $N_z=10$ ,  $V_z=2$  meV and  $m=0$ . The other parameters are taken as  $A_1=220$  meV·nm,  $A_2=410$  meV·nm,  $B_1=-100$  meV·nm<sup>2</sup>,  $B_2=-566$  meV·nm<sup>2</sup>,  $M_0=280$  meV [2]. Note that the parameters are different from that of antiferromagnetic MnBi<sub>2</sub>Te<sub>4</sub> because ferromagnetic TIs are made of TIs with magnetic dopants in recent experiments [3–5].